Novel Simulation Technique of Radioactive Aerosol Substances Propagation into the Motionless Atmosphere Suddenly Disseminated by Wind to Surrounding Environment

Petr Pecha[1], Miroslav Kárný[1]

pecha@utia.cas.cz, school@utia.cas.cz

[1] The Czech Academy of Sciences, the Department of Adaptive Systems of the Institute of Information Theory and Automation, v.v.i.
Pod vodárenskou věží 4, 182 00, Prague 8, Czech Republic.

Abstract. Accidental discharges of radioactive aerosol into the motionless (calm) atmosphere are examined with aim to quantify ensuing radiological impact on population. This paper offers an advanced methodology that facilitates and accelerates the demanding modelling process in the calm region. The modelling simulates continuous, quite volatile, radioactive releases under strong variations of the atmospheric conditions by a chain of discrete Gaussian pulses. An original idea of insertion of the nested inner cycle enables to comprise the atmosphere state changes during individual pulse propagation. The radioactivity concentration in air at the calm end period becomes a quite non-Gaussian sum of the Gaussian puffs. The novel processing provides a simple and sufficiently precise estimate of its statistical properties. The processing approximates the sum by a single "super-puff" distribution of the Gaussian type. It remarkably facilitates analysis of the ensuing convective transport of the radioactivity package. Instead of many calculating runs of the convective transport for each individual puff, only one run realises. The approximation is based on Bayes' paradigm (*AB*). The numerical experiments confirm the acceptability of the *AB* procedure under the inspected circumstances. The proposed way converts the laborious modelling of radiological fields into a feasible one. It supports practicability of the sampling based methods of uncertainty and sensitivity analyses, as well as the data assimilation methods, especially their inverse modelling techniques based on simulation of multiplex radiological trajectories.

Keywords: calm atmosphere, aerosol dispersion and deposition, pollution dissemination, hot spot occurrence, non-Gaussian sum, Kullback-Leibler divergence, Gaussian approximation

1 Introduction

Mankind needs to reduce and minimize the impact of environmental disasters like earthquakes, volcanic eruptions, wild-land fires, sand and dust storms or biological emergencies. In the same line, the disasters from human activities have immediate impact on population. Various threats adversely influence the critical infrastructures. They concern energy generation and distribution, chemical production and distribution, transportation systems, agriculture production (pollen and odour transport, pesticide dispersion, greenhouse gases propagation) and other. Accidents connected with discharges of chemical and radioactive substance harm human health and the environment. Chemical-plant failures or traffic accident during transport of chemicals are frequently described and documented. Chlorine or ammonia gas leak from an industrial facility or spill from broken truck during transport accident threat the adjacent population. Similarly, discharges of hydrogen sulphide from a tanker or massive releases of bromine gas into the atmosphere were reported. Probably the world's worst industrial disaster, with approximately 2500 death, caused by methyl isocyanate poisoning due to leaking from a storage tank, happened in Bhopal, India, 1984. In response to the catastrophic incidents, improvements of safety regulations for the use and

distribution of the hazardous chemicals have been introduced. A similar progress in nuclear safety has been directed after the nuclear catastrophe in Chernobyl and the Fukushima accident. Disaster preparedness must also account for terroristic attacks spreading the harmful chemicals or radioactive substances into the environment. Emergency readiness plans should include management of the radiological consequences of attacks via atmospheric dispersion of contaminants originating from, for instance, 'dirty bomb' explosions. A special attention should be given to the accidents during worst-case meteorological conditions. We care about such particular atypical, rarely addressed, cases, of serious radioactivity spreading under very low wind speed conditions. Within this scenario, a novel technique is designed that speeds up evaluations and is applicable to other cases, too.

Hazardous effects of accidental radioactive releases during an atypical episode of the low wind speed state are examined. A hypothetic but realistic experiment is carried out with a radioactivity in the aerosol form accidentally released into the motionless atmosphere. During a few hours of the calm state, dangerous radioactivity values may locally accumulate. The calm state is immediately followed by the windy convective transport that disseminates the hazardous aerosol material. Notably, the hot spots of deposited ^{137}Cs occur when the scenario is combined with the atmospheric precipitation. The hot spots exhibit a significantly increased radioactivity deposited on the ground. The presented modelling proposes and verifies its novel fast numerical treatment.

The topic of the paper concerns thoroughly inspected domain. Inevitably, a classical material is repeated in order to make the paper as much self-containing as possible and to explain practical important technical details.

Sec. 2 models the considered release scenario. The inspected realistic low wind speed and calm conditions origin from the data provided by the Czech meteorological service. The archived hourly meteorological data forecasted for a nuclear power-plant locality has served for assessing the probability of occurrence and the average duration time of the calm episode. The inspected mathematical model uses a superposition of discrete Gaussian puffs labelled by $m \in \{1,...,M\}$ that are released from an elevated resource. The superposition approximates any continuous radioactive release. Each puff evolves during consecutive windless stages within a calm region. Afterwards, it spreads due to the ensuing convective transport initiated by the wind. Parameter changes in the calm region can account for the release source strength, isotopic composition, atmospheric stability class, rainfall, and release height. The computation scheme comprises a detailed nested propagation model of the m^{th} puff. From its birth until the calm end, the puff propagates during adjacent time intervals. The model copes with the forthcoming changes of atmospheric stability class, *e.g.* in *(Hanna et al., 1982)*, or atmospheric precipitation. The radioactivity depletion due to the radioactive decay, aerosol dry activity deposition and washout of aerosol by a prospective rain is respected. Depletion factors reflecting the radioactive decay, aerosol dry and wet radioactivity depositions are discussed for the calm episode. Sec. 4.2 adjusts them for the convective region.

Sec. 3 expands and generalizes a novel pollution processing introduced in *(Pecha et al., 2020)* for earlier minor release scenario and lower experiment dimensionality. It is applied just after the calm period end and initiates the convective radioactivity transport. This speeds up evaluations much and makes them widely applicable. Instead of processing all puffs further on (brute-force solution, *BF*), the non-Gaussian mixture of radioactivity concentrations in the air at the calm episode end is replaced by a representative Gaussian distribution. The used and recalled approximation principle is motivated by Bayesian paradigm *(Bernardo, 1979)*. It relies on the fact that the Kullback-Leibler divergence, *(Kullback and Leibler, 1951)*, is the adequate proximity measure between the approximated

distribution and its approximant. The best Gaussian approximant is constructed. The solution is referred as the approximation based on Bayes' paradigm (*AB*).

Sec. 4 models the convective transport in *BF* or *AB* modes. Elementary Gaussian puff dispersion model is applied over short distances. It demonstrates the main features of the scenario and its solution. It points to the dangerous accumulation of radioactivity during the calm conditions and shows of the feasibility of the *AB* solution. The employed relevant dry deposition and wet washout parameterisations are compiled from fields' experiments.

The approximated sum of puffs gained by *BF* technique is clearly non-Gaussian. Numerical results of Sec. 5 experimentally support the use of the fast *AB* solution against accurate but slow *BF* way. The inspected hypothetical scenario consists of five hours of the calm episode succeeded by four hours of the convective transport. The rain occurs in the last fourth hour of the convective propagation. The calm interval is split into M segments, the variants with values $M \in \{6, 10, 100, 200, 300\}$ are examined. The source strength is assumed constant during the whole calm period. For $M=100$, the scenario with a serrated shape of discharges is also inspected. Comparisons of *BF* and *AB* solutions are made in the critical rainy convective phase. The results of both processing are in a good agreement. The experiments also show that the limit of the continuous discharges ($M \to \infty$) is well estimated.

The benefits demonstrating improved feasibility of joint uncertainty and sensitivity analyses performance of the CALM scenario are confirmed in the detailed complementary study *(Pecha and Kárný, 2021)* based on random sampling techniques.

2 The modelled accident conditions and the used modelling way

Potentially dangerous atmospheric dispersions at low wind speed state are inspected for a long time, see e.g., *(Jones, 1996), (Lines and Deaves, 1997), (Okamoto et al., 1999), (Hyojoon et al., 2013).* Performance evaluation and comparison of modified Gaussian and Lagrangian models under low wind speed is given in *(Rakesh et al., 2019).* Commonly large effect of the low wind speed variability on radioactivity concentrations in air are analysed in *(Pandey and Sharan, 2019).* Concentration measurements from the low wind diffusion field experiments are used for the qualitative performance of AERMOD code. A special technique of radiation distribution mapping on the ground can be realize using unmanned aerial vehicle (*Zhang et al., 2018*). Gained experience is utilised for simulation of the inspected radioactivity release scenario.

2.1 Low wind speed state

Continuous release having potentially strong changes of the release dynamics of the harmful aerosol substances is simulated by a long sequence of short-term instantaneous discharges (puffs). The release proceeds under zero horizontal wind speed. Each puff has a shape of an expanding discus with its centre at the pollution source. 3-D Gaussian-puff distribution describes the radioactivity concentration in the air. Time-dependent empirical relations gained from the field measurements under low wind speed serve for expressing its vertical and horizontal dispersion coefficients. The radioactivity depletion from the air caused by physical mechanisms is implemented. At the calm end, the resulting distribution is the superposition of all puffs having their own "age". The age is the travel time of the puff from its birth until the calm period end.

We take atmospheric conditions as "low wind" for wind speed $u < 0.5\ m.s^{-1}$. Our considerations relate to the low wind speed episodes include observations both from UK Meteorological Office (e.g. locality Herstmonceux over the 10-year period 1981-1990) and long-term meteorological records for territory of the Czech Republic. We have analysed series (period 5 years) of the archived hourly meteorological data forecasted for the points of the nuclear power plant (NPP) localities provided by the Czech hydro-meteorological service.

Long-term meteorological records in the Czech Republic assess the probability of occurrence of such low wind episodes up to 14%. The duration of low wind state fluctuates between tens of minutes up to several hours. A detailed analysis of the hourly meteorological data forecasted for the nuclear power plant localities has been carried out. The analysis in (*Pecha et al., 2020)* picks out the sequences with at least three consecutive data records, i.e. the low wind speed state lasting at least *3* hours. It was found that occurrence of uninterrupted calm sequences within the whole year longer than 10 ~ 20 hours is very improbable. We assume this longer sequences as unrealistic and out of our considerations. One of such sequences with the duration of *5* hours is shown in Tab. 1. Atmospheric stability classes categorise the extent of atmospheric turbulence, *(Kahl and Chapman, 2018)*. The stability class *F* stands for the stable conditions with at most slight incoming solar radiation and with the vertical temperature gradient from *1.5* to *4.0* degrees (usual night-time conditions).

Tab. 1: Archived meteorological data at (49° 05′ 00.73″ N, 16° 07′ 26.95″ E) of the Dukovany nuclear power plant: start at Dec 3, 2019, 20.00 CET (time_stamp 2019120320).

time_stamp yyyymmddhh	Pasquill_cat. - (**)	wind_speed at 10 m height[m.s^{-1}]	wind_direction [°](*)	rain [mm.h^{-1}]
.....	.....	.....	.....	.....
2019120319	.....	.....	.....	.....
2019120320	**F**	**0.2**	**343**	**0**
2019120321	**F**	**0.3**	**209**	**0**
2019120322	**F**	**0.2**	**122**	**0**
2019120323	**F**	**04**	**72**	**0**
2019120400	**F**	**0.4**	**309**	**0**
2019120401	.....	.....	.....	.....

(*) Clockwise, from the North; (**) Pasquill atmospheric stability class

The adopted definition of the calm state is a bit ambiguous and should be clarified. Fig. 1 illustrates our choice and reflects Tab. 1. It assumes that the aerosol particle No. 1 born at 2019120320 drifts around the source during five hour period. Its trajectory begins at source and terminates after 5 hours at position 1. It is marked by asterisks. Similarly, the trajectories of aerosol particles No. 2, 3, 4, 5 end at the points 2, 3, 4, 5 after 4, 3, 2, 1 hours, respectively. All drawn trajectories stay quite close, $\approx 500\ m$, to the release point during the interval <2019120320; 2019120400>. This shows that the cases with the wind speeds $u < 0.5$ m.s^{-1} even during five hour period well approximate the calm state with reference wind speed $u = 0\ m.s^{-1}$. At very low wind speeds, the pollutant exhibits more or less chaotic fluctuations and stays close to its source.

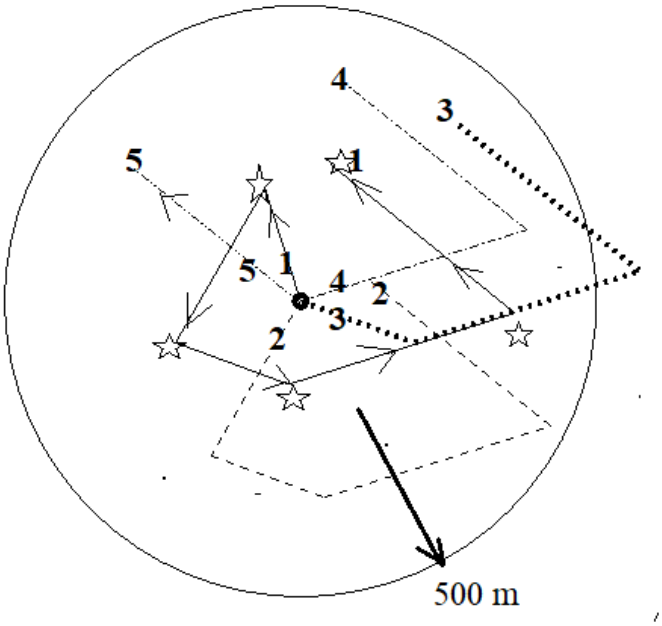

Fig. 1: Trajectories of five aerosol particles discharged at the source according the time stamps from Tab. 1. The depicted situation is just after the fifth hour 2019120400 (Dec 04, 2019).

2.2 Comments on mathematical models of low wind speed episodes

The modelling of low wind speed dispersion can be theoretically treated as a continuous release, traditionally described by segmented Gaussian dispersion models. It was believed that the steady-state Gaussian dispersion models, such as AERMOD, *(EPA, 2004)*, or ADMS, *(Carruthers et al., 2003)*, are not applicable when the wind speed near the ground is comparable to the standard deviation of the horizontal velocities. The performance of the Gaussian dispersion models is poor and the concentration values during such episodes are overestimated. Some approximations were proposed for solving this problem. The most important one addresses the overestimation. It was shown that low-frequency meandering occurs whenever the wind speed is below $2.0\ m.s^{-1}$. The approximation increases minimum horizontal turbulence and incorporates a modified meander component. The comparison with application of Lagrangian dispersion model *(Rakesh et al., 2019)* has found a good agreement of the Gaussian model results with the improved dispersion parameters.

Profound overview of the key references and methodological progress are in *(Pandey and Sharan, 2019).* The segmented plume approach with all new options is recommended there as a good modelling way. Accountability of the wind variability in AERMOD code for computing concentrations under low wind state is assessed. The effect of low wind conditions and wind intervals are treated in *(Hyojoon et al., 2013).* The influence of definition of the calm conditions (wind speed $< 0.5\ m.s^{-1}$) and classification of the low wind speed ($< 2.0\ m.s^{-1}$) on atmospheric dispersion factors using a Gaussian plume model is documented here. The study used meteorological data measured in one hour intervals. *(Lines and Deaves, 1997)* examine the implications of dispersion in low wind state for a qualified risk assessment.

In summary, the low wind speed ($< 2.0\ m.s^{-1}$) analysis based on the segmented plume approach with all new options suits for modelling of dispersion of a pollutant under these conditions. Extra small wind speed ($< 0.5\ m.s^{-1}$) with chaotic fluctuations is classified as calm conditions (in the sense of Fig. 1 above) and they are examined onwards.

2.3 An approximation of radioactivity release into calm air by discrete discharges

Impacts of release of radionuclides during the calm conditions are treated as a superposition of a chain of Gaussian puffs from the elevated source. Each puff has its own nuclide inventory and its strength of the released activity. The state of the puff in the calm region reflects a local actual state of atmospheric stability and possible immediate atmospheric precipitation.

Vertical and horizontal dispersion coefficients are expressed by time-dependent empirical relations suggested in *(Okamoto et al., 1999), (McGuire et al., 2007).* Time evolution of each puff reflects the depletion of the activity due to radioactive decay, dry activity deposition on the ground, and washout due to the atmospheric precipitation. The removal mechanisms are incorporated into analysis via so called "source depletion" factors.

Fig. 2 shows the modelling scheme. The release dynamics of radioactivity during the leak time period $< T_{START}^{LEAK} ; T_{END}^{LEAK} >$ is simulated by a chain of discrete puffs of strengths Q_m^n [Bq]. They are ejected stepwise at starts of adjacent regular time periods $\Delta t_m, m \in \{1,\ldots,M\}$.

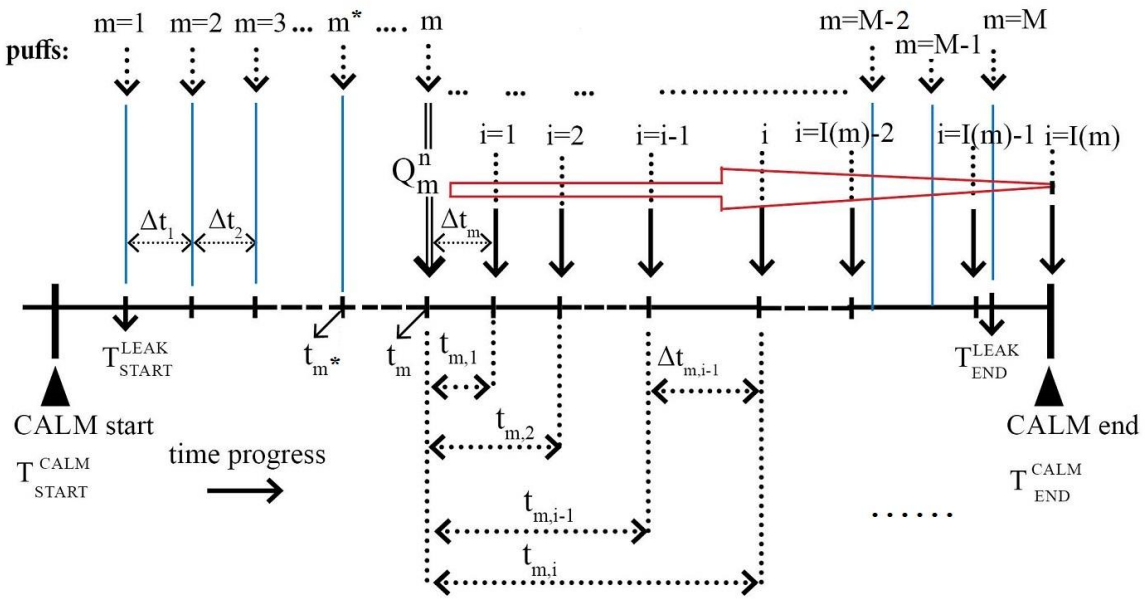

Fig. 2: Detailed scheme of the time progress of discrete radioactivity discharges into the motionless ambience during a calm meteorological episode. Propagation of the individual discharge Q_m^n [Bq] of the puff m from its birth at time t_m until end of the calm situation T_{END}^{CALM} is modelled with nested cycle i accounting for impact of stepwise changes of meteorological situation on the puff m travelling onward.

The proposed original algorithm discerns two kinds of the scenario parameters. Firstly, both variable inventory of the leaking radionuclides and the dynamics of the release source strength should be reflected within the construction of Q_m^n. The puff has its own unique properties as radionuclide content, aerodynamic diameter and particle shape of the aerosols, heat capacity, etc. Secondly, the discharge Q_m^n of the pulse m during its propagation from the

birth at time t_m until the end of calm T_{END}^{CALM} is submitted to variations of the atmospheric state (changing atmospheric precipitation, variations of atmospheric stability category modifying dispersion coefficients in the air). The changes run stepwise in the nested cycle $i \in \{1,\ldots, I(m)\}$ (see Fig. 2, i numbers the time relatively to the m^{th} puff birth). The source strength from the elevated source at a height H $(x=0;\ y=0;\ z=H)$ in the time interval Δt_m is denoted $S_m^n(t)$ [Bq.s^{-1}]. It specifies the discharge of radioactivity Q_m^n assigned to Δt_m according

$$Q_m^n = \int_{(\Delta t_m)} S_m^n(t) \cdot dt\,. \tag{2.1}$$

It is treated onwards as an instantaneous impulse ejected at the beginning of the interval Δt_m. We assume that M discrete puffs of the n^{th} radionuclide are released from the same elevated point source at a height H inside the mixing layer during the calm episode within the time interval $\left\langle T_{START}^{CALM}\,;\, T_{END}^{CALM}\right\rangle$. The first puff starts at the beginning of the accident T_{START}^{LEAK}, the last puff $m=M$ starts at its end T_{END}^{LEAK}. The "age" of the m^{th} puff at the end of the relative interval i is $t_{m,i} = \sum_{k=1}^{k=i} \Delta t_{m,k}$ (see Fig. 2).

The activity concentration $C^n\left(t\,;x,y,z\right)$ [Bq.m^{-3}] of the n^{th} radionuclide in the air is described by 3-D Gaussian puff formula, see *(Zannetti, 1990)* or *(Carruthers et al., 2003)*. We model its evolution under simplifying assumptions. We assume stable conditions and no inversion. The solution considers only one reflection from the ground plane. The puff shape is symmetrical in the x and y directions. Thus, these coordinates are replaced by the horizontal distance r from the centre of the puff. The further formalisation follows from the notions summarised in Fig. 2.

The puff of the strength Q_m^n [Bq] of the n^{th} radionuclide born at the beginning of m^{th} interval at time t_m propagates through the adjacent time intervals marked by i relative to m. The used stepwise modelling assumes that for each interval i the puff "stays on" here for the time period $\Delta t_{m,i}$. It is submitted to the specific stepwise atmospheric conditions (precipitation, stability class) expressed by index i. Relative time $t \in \langle 0,\ \Delta t_{m,,i} \rangle$ is used, cf. Fig. 2. The symbol $C_{m,i}^n(t; r, z)$ stands now for the radioactivity concentration in the m^{th} puff within the subinterval $\Delta t_{m,i}$. We label $\tilde{t}_{m,i}\,(t) = t_{m,i-1} + t$ as the propagation time of the m^{th} puff from its birth until $t_{m,i-1} + t$. The concentration shape within this interval gets the form

$$C_{m,i}^n(t; r, z) = \frac{Q_{m,i}^n(t)}{(2\pi)^{3/2} \cdot \sigma_r^2\left(\tilde{t}_{m,i}(t)\right)} \cdot \exp\left(-\frac{r^2}{2 \cdot \sigma_r^2\left(\tilde{t}_{m,i}(t)\right)}\right) \times \tag{2.2}$$

$$\times \frac{1}{\sigma_z^2\left(\tilde{t}_{m,i}(t)\right)} \cdot \left\{ \exp\left(-\frac{(z - h_{ef,m})^2}{2\sigma_z^2\left(\tilde{t}_{m,i}(t)\right)}\right) + \exp\left(-\frac{(z + h_{ef,m})^2}{2\sigma_z^2\left(\tilde{t}_{m,i}(t)\right)}\right) \right\}$$

The expression (2.2) exploits the assumed symmetry and the assumption of a single reflection from the ground level. This implies the equality of the standard deviations $\sigma_x = \sigma_y = \sigma_r$ at the distance r, $r^2 = x^2 + y^2$. In (2.2), the puff strength at the time t is

$$Q_{m,i}^n(t\ ) = Q_m^n \cdot f_R^n(t_m \to \tilde{t}_{m,i}(t)) \cdot f_F^n(t_m \to \tilde{t}_{m,i}(t)) \cdot f_W^n(t_m \to \tilde{t}_{m,i}(t))\,. \tag{2.3}$$

The Eq. (2.3) expresses the "source depletion" scheme. It is driven by the combined depletion factors f_R^n, f_F^n, f_W^n for radioactive decay, fallout on terrain and washout by the rain. They represent the radionuclide depletion from the time of birth until the true time of propagation. The depletion factors are briefly discussed below. A discussion and comparison of the "source depletion" with an alternative "surface depletion" approach is e.g. in *(Horst, 1977).*

2.4 Depletion of stationary puff due to radioactive decay

Radioactive decay happens within the entire puff volume. The corresponding depletion within the time interval $<t_0; t>$ is proportional to $\exp[-\lambda\cdot(t-t_0)]$ with $\lambda>0$. Specifically, the depletion factor of the original puff *m* of radionuclide *n* from its birth up to the end of its relative time interval *i* is

$$f_R^n\left(t_m \rightarrow t_{m,i}\right) = \prod_{k=1}^{k=i} \exp\left(-\lambda^n \cdot \Delta t_{m,k}\right) = \exp\left(-\lambda^n \cdot t_{m,i}\right) \tag{2.4}$$

where λ^n [1/s] is the constant of the radioactive decay specific to the n^{th} radionuclide.

2.5 Depletion of stationary puff due to dry deposition (fallout)

Depletion of the puff activity concentration due to dry deposition follows from the interaction with the surface layer and the gravitational settling. Smaller aerosol particles of the size in the range $<0.1, 1>$ μm survive for a long time. Their depletion from the plume is mainly caused by interaction with the surface structures. It depends on the surface roughness and friction velocity. The gravitational settling speed varies and depends on the atmospheric stability, the wind speed and the surface conditions.

For the calm conditions, we can focus on gravitational settling of aerosol particles, which have an important role in the radiological hazard. The settling process is significant for particles of higher diameter values, which do not remain airborne for a long time. A brief summary of gravitational settling is, e.g., in *(Hanna et al., 1982), (Pollanen et al., 1995), (Baklanov and Sorensen, 2001).*

For relative time $t \in < 0, \Delta t_{m,k} >$, we search for the total activity in the m^{th} puff $Q_{m,k}^n\left(t_{m,k-1} + t\right) \in \left\langle Q_{m,k}^n\left(t_{m,k-1}\right), Q_{m,k}^n\left(t_{m,k}\right)\right\rangle$. The near-ground activity concentration $C_{m,k}^n\left(t; r, z=0\right)$ depletes according to Eqs. (2.2) and (2.3). The total dry deposition flux of the m^{th} puff of the n^{th} nuclide on the ground $\dot{\Omega}_{m,k}^n\left(t; z=0\right)$ [Bq/s] at time *t* is

$$\dot{\Omega}_{m,k}^n\left(t; z=0\right) = \int_0^\infty v g_{grav}^n \cdot C_{m,k}^n\left(t; r, z=0\right) \cdot 2\pi \cdot r \cdot dr \tag{2.5}$$

The near-ground activity concentration $C_{m,k}^n\left(t; r, z=0\right)$ from Eq. (2.2) is substituted here. The source strength reduction in the interval $\Delta t_{m,k}$ due to the deposits on the ground is expressed as

$$dQ_{m,k}^n\left(t\right)/\, dt = -\dot{\Omega}_{m,k}^n\left(t; z=0\right). \tag{2.6}$$

After substitution from Eq. (2.2), the final time integration is conducted in the interval $< t_{m,k-1}$, $t_{m,k} >$. It gives the partial depletion factor $f_F^n(\Delta t_{m,k})$ on the interval $\Delta t_{m,k}$. The final total dry-deposit-depletion factor for the m^{th} puff from its birth until the i^{th} time interval is

$$f_F^n(t_m \to t_{m,i}) = Q_{m,i}^n \Big/ Q_m = \prod_{k=1}^{k=i} f_F^n(\Delta t_{m,k}) \tag{2.7}$$

This expression is here motivated qualitatively. More detailed derivation is in *(Pecha et al., 2020).* Analysis in *(Tsuda et al., 2013)* deeply studied the sedimentation velocity as a function of the particle aerodynamic diameter, particle shape, particle composition, surface characteristics, charge or possible coagulation processes. Here, the roughly estimated value $vg_{grav}^n = 0.008$ m.s^{-1} is used. It can be accepted for aerosol particles with radii about *5-10* μm. With it, the integration of (2.5) over the period $\Delta t_{m,i}$ provides the resulting total activity of n^{th} radionuclide deposited on the ground during the period $\Delta t_{m,i}$ due to fallout.

2.6 Wet deposition from stationary puff (washout)

The release scenario under rainy weather with a constant precipitation intensity lasting the whole calm period is analysed. The radioactivity concentration $C_{m,k}^n(t; r, z)$ of the n^{th} radionuclide in the m^{th} puff, born at the time moment t_m, during its k^{th} stage is expressed by Eq. (2.2). We search for the total activity distribution in the puff $Q_{m,k}^n(t) \in \langle Q_{m,k-1}^n, Q_{m,k}^n \rangle$ [Bq] within this interval; t means relative time variable $t \in < 0, \Delta t_{m,k} >$ in a rainy interval $\Delta t_{m,k}$. The activity concentration $C_{m,k}^n(t\,; r, z)$ for $t \in < 0, \Delta t_{m,k} >$ is gradually depleted by washout. The assumed precipitation rate of the rain $\upsilon_{m,k}$ [mm/h] is constant during the entire interval $\Delta t_{m,k}$. The deposition activity rate of the n^{th} radionuclide being washed out from the cloud is expressed using washing coefficient $\Lambda_{m,k}^n = a \cdot (\nu_{m,k})^b$ [1/s]. The constants a, b depend on the physical-chemical form of the radionuclide. They are different for aerosol, elemental, organic form, and zero for noble gases. The total wet deposition flux $\dot{W}_{m,k}^n(t)$ [Bq/s] from the m^{th} puff in its k^{th} time interval is given by

$$\dot{W}_{m,k}^n(t) = \int_0^\infty \left[\Lambda_{m,k}^n \cdot \int_0^\infty C_{m,k}(t; r, z) \right] \cdot 2\pi \cdot r \cdot dr \quad . \tag{2.8}$$

The activity concentration $C_{m,k}^n(t; r, z)$ from Eq. (2.2) is substituted here. The source strength reduction on the interval $< 0, \Delta t_{m,k} >$ due to the wet deposition on the ground reads

$$dQ_{m,k}^n \big/ dt = -\dot{W}_{m,k}^n \,. \tag{2.9}$$

After substitution, the final integration is conducted over the time interval $< t_{m,k-1}$, $t_{m,k} >$. This gives the depletion factor $f_W^n(\Delta t_{m,k})$ on the partial interval $\Delta t_{m,k}$. The final form of the total washout depletion factor for the m^{th} puff from its birth until the i^{th} time interval is

$$f_W^n(t_m \to t_{m,i}) = Q_{m,i}^n \Big/ Q_m = \prod_{k=1}^{k=i} f_w^n(\Delta t_{m,k}) \tag{2.10}$$

Let us stress that for discontinuous rain episodes, the algorithm should be re-adjusted. In brief, several combinations can be considered, for example:

– During propagation of the m^{th} puff, let precipitation occurs only within a partial interval $\Delta t_{m,i}$. Washout depletion factor $f_W^n\left(\Delta t_{m,i}\right)$ can be found and substituted into (2.10). All other partial factors equals 1.0 (no rain). Furthermore, a bit more complex scheme should account for the previous adjacent puffs *m-1*, *m-2*…. that were discharged before the rain shower and so far not reaching T_{END}^{CALM} . Let assume a certain previous puff $m*$, $m* < m$. Following Fig. 2, this puff $m*$ enters the speculated rainy interval $\Delta t_{m,i}$ at time $((t_m - t_{m*}) + t_{m,i})$ from its birth at t_{m*} and the partial washout of the puff $m*$ is found.

– If a long-lasting rain starts at the beginning of the m^{th} puff, the previous puffs $m* < m$ are already "on the road" in their respective phases $i(m*)$ (relative to the $m*^{th}$ puff birth). Then, we have to consider the relative phase $i(m*)$ of the puff $m*$ as wet (washed out) provided that $t_{m*,i(m*)} > (t_m - t_{m*})$.

Other variations of the rain occurrence can be adjusted provided that reasonable terms of splitting of the relative aggregations $i(m)$ and $i(m*)$ are adequately respected.

3 Evaluation of Radiological Quantities just at the Calm Episode Termination T_{END}^{CALM}

The radioactivity accumulated in the stationary ambient atmosphere is a superposition of results of all partial puffs m until they reach end of the calm period T_{END}^{CALM} . The total radioactivity concentration in the stationary package of air at the time T_{END}^{CALM} is expressed as sum

$$C^n\left(T_{END}^{CALM};r,z\right)^{TOTAL} = \sum_{m=1}^{m=M} C_{m,I(m)}^n(r,z). \qquad (3.1)$$

$C_{m,I(m)}^n(r,z)$ is concentration of the puff m (born at time t_m), which reached the end of the calm period just at the moment T_{END}^{CALM} (according to the scheme in Fig. 2). The puff m runs stepwise within the nested cycle $i \in \{1,\ldots, I(m)\}$, index $I(m)$ corresponds to T_{END}^{CALM} . Eq. (3.1) superposes multiple Gaussian puffs. Each puff reflects a partial discharge of the radioactivity Q_m^n, $m \in \{1,\ldots,M\}$, which dissipates into the motionless ambient atmosphere just until to the calm-period termination. The results of current realistic calm scenario analysed here are displayed on Figure 3a (large number $M=100$ of discharged puffs during total calm duration $T^{CALM} = 5$ *hours*). For comparison, the results of former hypothetical minor calm scenario examined recently in (*Pecha et al., 2020*) are displayed on Figure 3b (smaller total number of discharged pulses $M=6$ during total calm duration period $T^{CALM} = 2$ *hours*). The values on Figs. 3 are normalised to the same value *6.0 E+07 Bq* of the total radioactive discharge Q_{TOT}^n given below by Eq. (5.1).

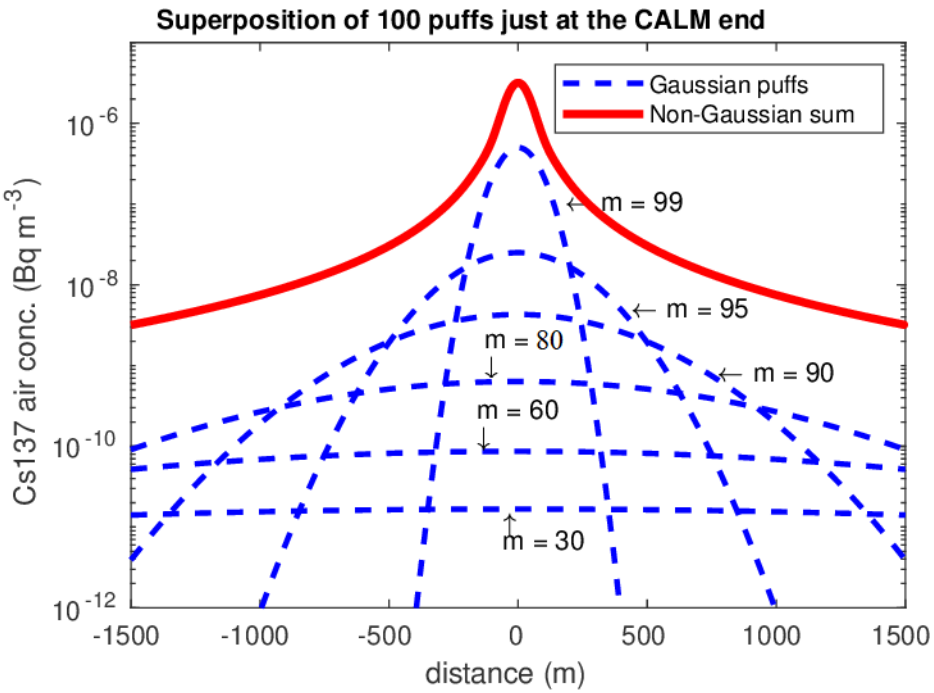

Fig. 3a: Specific radioactivity of ^{137}Cs in air, all values related just to the end of the calm situation T_{END}^{CALM} . Composition of resulting non-Gaussian distribution (given by Eq. (3.1) - unbroken line) from the individual discrete Gaussian puffs $m \in \{1,\ldots,M\}$; *M=100* (dashed lines). Duration of the calm episode T^{CALM}*=5 hours*. Other parameters – see Sec. 5, below.

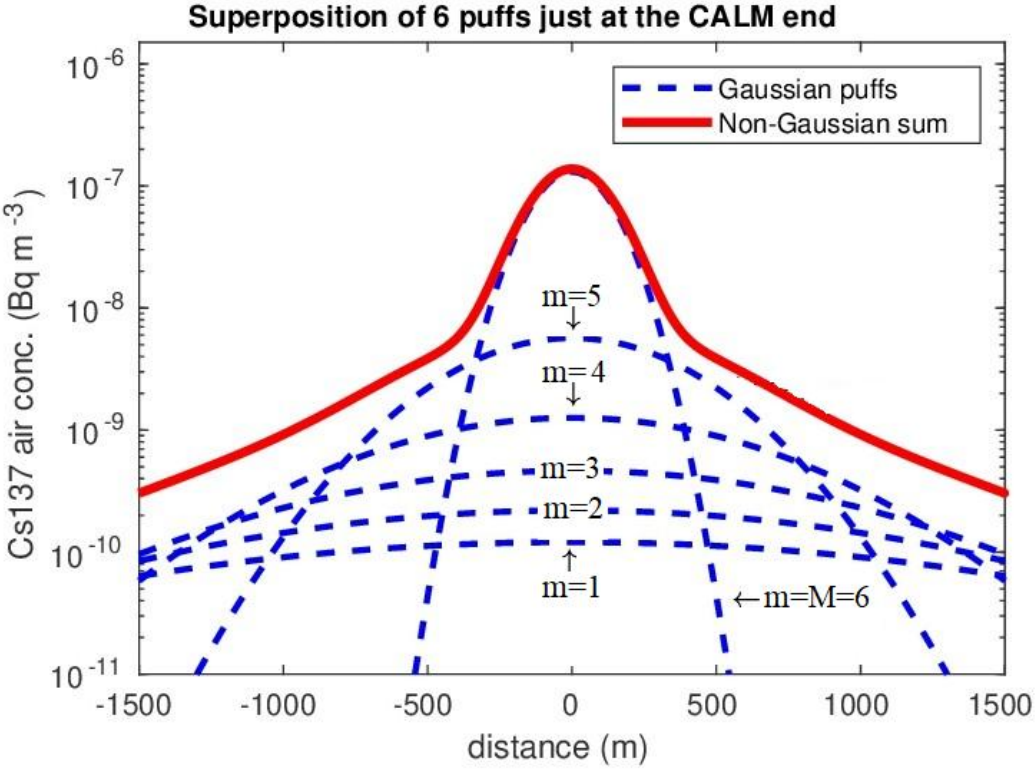

Fig. 3b: Similar results as on above Fig. 3a for analysis of minor calm scenario from *(Pecha et al., 2020)*. Specific radioactivity of ^{137}Cs in air, all values related just to the end of the calm situation T_{END}^{CALM} . Composition of resulting non-Gaussian distribution (given by Eq. (3.1) - unbroken line) from the individual discrete Gaussian puffs $m \in \{1,\ldots,M\}$; $M=6$ (dashed lines); Duration of the calm episode $T^{CALM}=2$ *hours*.

Modelling flexibility requires a high number of puffs M, which induces high processing demands. It is desirable to decrease the puffs' amount whenever the need for a high number of puffs is less urgent. A further processing is prepared for a sum of Gaussian puffs. Thus, the superposition (3.1) has to be approximated by a superposition with a smaller number of terms. The next section justifies the chosen approximation way.

3.1 The approximation principle

AB processing requires a specification of: a) the divergence measure between the approximated function and its approximant; b) the class of approximants where the best one is searched for. The divergence measure is chosen here, the approximants in the next subsection.

The approximated function (3.1) is non-negative and its physical meaning implies that it has a finite integral. Thus, it is proportional to a probability density function $P(r, z)$, which is a weighted sum of Gaussian probability density functions. It should be approximated by another probability density function $G(r,z)$ of a simpler form. Works *(Bernardo, 1979)* and *(Kárný and Guy, 2012)* shown that under different, but quite general, conditions the Kullback-Leibler divergence, *(Kullback and Leibler, 1951)*,

$$KL(P,G) = \iint P(r,z) \ln\left(P(r,z)/\,G(r,z)\right) dr\, dz \tag{3.2}$$

are the (only) adequate proximity measure. The optimal approximant G^{opt} is then found in the set $\boldsymbol{G}$ of candidates

$$G^{opt} \in Arg\min KL(P,G); \quad \in \boldsymbol{G} \tag{3.3}$$

Importantly, the optimised divergence and thus the optimum are invariant with respect to a regular transformation of coordinates.

3.2 The choice of the set of approximants

Figs. 3 demonstrate that the superposition of all partial puffs M is clearly non-Gaussian. Thus, the set $\boldsymbol{G}$ in (3.3) should consist of mixtures of Gaussian pds having less than M terms but more than one, *(McLachlan and Peel, 2000)*. This ideal case, however, makes evaluation of the Kullback-Leibler divergence (3.2) and thus minimisation (3.3) quite demanding, *(Hershey and Olsen, 2007)*. This has led us to the attempt to approximate the mixture by a single Gaussian probability density function. Experimental part of the paper confirms success of this attempt to estimate the statistical properties of $C^n\left(T_{END}^{CALM};r,z\right)^{TOTAL}$ by substituting the Gaussian mixture (3.1) with one Gaussian super-puff. This allows us to predict well and quickly a further convective transport of the potentially dangerous radioactivity accumulated during the calm period and to predict its radiological impact.

3.3 The best Gaussian approximant

If the approximants' set ***G*** contains Gaussian probability density functions

$N(\mu,\rho;r,z)=|2\pi\ \rho|^{-0.5}\ \exp\left\{-0.5([r,z]-\mu)\ \rho^{-1}([r,z]-\mu)^{\dagger}\right\}$ † marks transposition,

it is simple to find the best approximant G^{opt} (3.3). It has the expectation μ^{opt} and covariance matrix ρ^{opt} equal to those of the approximated mixture $G(r,z)=\sum_{(m)}\alpha_m\ N(\mu_m,\rho_m;r,z)$,

where μ_m, ρ_m are the initial moments of the m^{th} puff. The probabilistic weight $\alpha_m \in \langle 0;1\rangle$, $\sum_{(m)}\alpha_m=1$, is a relative weight of this puff in the sum (3.1), i.e.

$$\alpha_m=\iint C_m(r,z)\,dr\,dz\ /\ \sum_m\iint C_m(r,z)\,dr\,dz\ ,$$

$$N(\mu_m,\rho_m;r,z)=C_m(r,z)\ /\iint C_m(r,z)\,dr dz \qquad (3.4)$$

The optimal Gaussian approximant $G^{opt}(r,z) = N(\mu^{opt},\rho^{opt};r,z)$ has the moments

$$\mu^{opt}=\sum_{(m)}\alpha_m\ \mu_m \quad , \quad \rho^{opt}=\sum_{(m)}\alpha_m\ (\rho_m+\mu^{\dagger}\ \mu_m)-(\mu^{opt})^{\dagger}\mu^{opt} \qquad (3.5)$$

Thus, the overall evaluation consists of: a) scaling (3.4) the approximated superposition (3.1) and its constituents to probability density functions; b) use formula (3.5); rescaling the resulting $G^{opt}(r,z)$ into

$$C^{opt}(r,z)=\left(\sum_{(m)}\iint C_m(r,z)\,dr\,dz\right)N(\mu^{opt},\rho^{opt};r,z),$$

so that the original overall concentration, evaluated during the normalisation, is preserved.

4 Ensuing Convective Transport of Previous Stationary Heap of Radioactivity

By assumption, a convective movement of the atmosphere immediately follows the calm episode. The wind starts to blow. It drifts and scatters the stationary heap of the radioactivity over the terrain. A fast and sufficiently accurate estimate of dangerous radiological impact on the living environment in vicinity of the radioactive source is needed. It plays a crucial role in the early introduction of the efficient countermeasures for the protection of inhabitants. Two scenarios exploiting the exact *BF* and approximated *AB* outcomes of the calm period processing is described below. Two auxiliary software subsystems have been constructed here for purposes of results visualisation and demonstration of basic principles of radioactivity propagation. Naturally, each emergency support centre has its own certified bunch of advanced dispersion models for regional use or long-range transport *(e.g. Park et al., 2017; Brioude et al., 2013).* But the main strength developed here for the case of calm scenario is introduction of the "super-puff" concept given by optimal Gaussian approximant $G^{opt}(r,z)$. Hypothetical release of harmful substances into the motionless atmosphere is lastly submitted by wind as the only approximated Gaussian package. It could be profitable for the advanced computationally expensive dispersion codes as an effective initial condition.

4.1 Model in summary

A basic simple formulation for small-scale advection of puffs under stable and neutral conditions is adopted here. The auxiliary algorithm serves only for demonstration of the novel features of the statistical approximation based approach *AB*[1]. The algorithm applied here evaluates the "source depletion" model of Gaussian puffs under the convective transport. Radioactivity propagation over the flat terrain is driven by stepwise hourly changes of meteorological data forecasted relative to the point of release. Atmospheric stability is characterised by Pasquill class[2]. In spite of these simplifications, a relevant picture of the main convective transport features can be outlined.

The puffs are assumed to be symmetrical in the *x* and *y* directions. These coordinates are replaced by the horizontal distance *r*. The centre of the puff is linearly moving in the wind direction. The relative diffusion with respect to the puff centre progresses. The Gaussian puff model is used. The available hourly changes in the meteorological state are segmented. Within each hour, the propagation goes along a straight line and all changes appear at once for the given hour. We focus on the near-field analysis in a small domain and below the mixing layer. Sophisticated, computationally more expensive, modelling accounting for a puff meandering or a puff furcation is prepared. The puff model with these limitations has been included in the bunch of the dispersion models of the HARP system, *(HARP, 2010-2019)*.

The radioactivity concentrations, determined either by $C^n_{m,I(m)}(r,z)$ from (3.1) for a puff *m* or from (3.4) for the single super-puff approximation, represent the initial conditions of the ensuing convective transport. Two alternative procedures of handling the considered convective transport are used:

Brute-force solution (*BF*): Movements of all individual Gaussian puffs $m \in \{1,..,M\}$ with the radioactivity concentrations $C^n_{m,I(m)}(r,z)$ from (3.1) are modelled through whole convective phase. The resulting radiological quantities are then given by superposition for all *M* puffs. The procedure provides an exact physical picture. A bulky demands on computer resources is its disadvantage. It may be killing for a high *M* well-modelling the calm phase.

Approximation based on Bayes' paradigm (*AB*): Statistical properties of the sum of all partial puffs $C^n\left(T^{CALM}_{END};r,z\right)^{TOTAL}$ given by (3.1) are projected on a representative Gaussian super-puff via (3.4). Unlike *BF*, it requires only one-shot run modelling the convective transport. The benefit of the reduced computational load is evident, especially for a large number of puffs *M* and prospective demands on necessary application of more powerful but laborious dispersion codes. The reduction is paid by the introduced approximation error. Its extent, experimentally studied in Sec. 5, seems to be acceptable.

4.2 Overview of simplified mathematical description of the convective transport

[1] In the real situations, some more efficient but computationaly demanding advanced dispersion codes will take advantages of the effective solution AB.

[2] More sophisticated Gaussian models (for instance, ADMS, *(Curruthers et al., 2003)* or AERMOD, *(EPA, 2004)*) use advanced parametrization of the atmospheric turbulence by the boundary layer depth and the Monin-Obukhov length, rather a single Pasquill class. Accounts for diurnal sensible heat flux changes. Among others, it allows to simulate the impact of complex hilly terrain, near-standing buildings or real physical schemes of dry and wet depositions.

Transport of radioactivity in convective hourly phases, labelled by *p*, follows. It applies further spreading either for a single puff *m* or single super-puff discharge of the *AB* solution. The individual discharge Q_m^n is gradually spreading inside the original calm region according to Fig. 2. The radioactivity concentration denoted in (3.1) as $C_{m,I(m)}^n(r,z)$ at the moment T_{END}^{CALM} can be rewritten as an equivalent expression $C_m^n\left(T_{END}^{CALM};r,z\right)$. At the same time, it is the initial condition for the first phase, *p=1*, of the convective transport. The original position of the previous calm region centre was (*x=0; y=0; z=H*). The convective movement in the direction $\vec{u}_1$ starts at T_{END}^{CALM} . The movement of the puff at each hourly phase *p* is composed of the absolute overall straight-line translations with the velocity values $\vec{u}_p$ and a relative dispersion around the puff centre. The dispersion parameters depend on the translation shifts. Available hourly meteorological data enables to account, step by step, for parameter changes reflecting the relevant scenario, see Fig. 4.

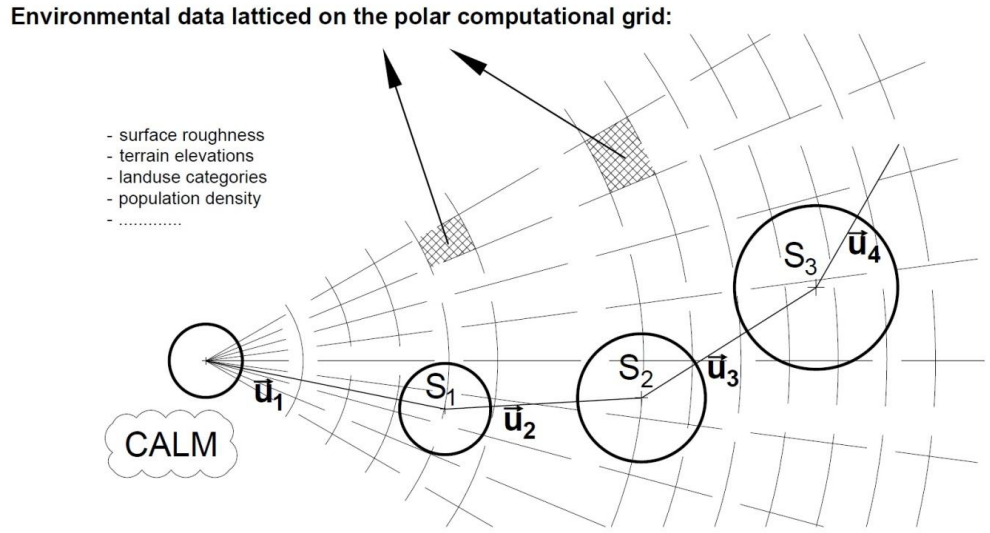

Fig. 4. Drift of the calm episode results in the ensuing convective flow. Each convective phase accounts for its specific environmental parameters. They are partially listed in the left upper corner.

The initial distribution of concentration of the m^{th} puff entering the first convective phase *p=1* is $C_m^n\left(T_{END}^{CALM};r,z\right)$. Sec. 2 specifies the depletion of the original discharge Q_m^n [Bq] from its birth at t_m until $t=T_{END}^{CALM}$. A similar description applies to the convective transport, but now the depletion depends on the distances passed along the puff trajectory. Real types of landuse and orography have to be respected. The parcel of radioactivity is successively drifted at hourly phases (intervals) *p=1, 2 ...* with the velocity values $\vec{u}_p$ and with other parameters of this scenario pertaining to the hourly changes. The radioactivity dispersion and depletion take place through the convective phases.

Let us inspect the movement of the m^{th} puff in its p^{th} convective phase. In the description, L_p stands for the puff zigzag trajectory from the start of convection entering (the phase *p=1*) up to beginning of the phase *p*. A relative distance *l* within the p^{th} phase concerns the interval $< 0;\ l_p >$. During the convective transport on the path length L_p+l, the discharge reduces by the composite depletion factor F_p^n, which reflects the puff progress:

$$F_p^n\left(L_p+l\right)= f_R^n\left(L_p+l\right)\cdot f_F^n\left(L_p+l\right)\cdot f_W^n\left(L_p+l\right). \qquad (4.1)$$

This accounts for all mechanisms of the activity removal pertaining to the convective ppf's transport. Indices *R, F, W* correspond to the radioactive decay, fallout, and washout. The dispersion coefficients $\sigma \in \{\sigma_r, \sigma_z\}$ are calculated individually as follows

$$\sigma(L_p + l) = \sigma(T_{END}^{CALM}) + \Delta\sigma(L_p + l); \quad \Delta\sigma(L_p + l) = \sum_{k=1}^{k=p} \Delta\sigma(l_k) + \Delta\sigma(l). \tag{4.2}$$

$\Delta\sigma(L_p + l)$ is the contribution to the dispersion along the total convective transport length L_p+l. It is evaluated either for smooth or, alternatively, rough terrain of the Central European land use for each phase *p*. $\Delta\sigma(l)$ stands for a dispersion increase in the interval $l \in < 0; l_p >$. The final expression for the activity concentration in the air within the p^{th} phase of the convective transport with the relative coordinate $l \in < 0; l_p >$ has the symbolic form, cf. (2.2),

$$C_{m,p}^{n}(l; r, z) = \frac{Q_m^n(T_{END}^{CALM})}{(2\pi)^{3/2} \cdot \sigma_r^2(L_p + l)} \times \exp\left(-\frac{r^2}{2 \cdot \sigma_r^2(L_p + l)}\right) \times \tag{4.3}$$

$$\times \frac{1}{\sigma_z(L_p + l)} \cdot \left\{ \exp\left(-\frac{(z - h_{ef,m})^2}{2 \cdot \sigma_z^2(L_p + l)}\right) + \exp\left(-\frac{(z + h_{ef,m})^2}{2 \cdot \sigma_z^2(L_p + l)}\right) \right\} \cdot F_p^n(L_p + l).$$

(r, z) are the coordinates relative to the centre of the puff, $\sigma(L_p + l)$ is given by (4.2), $F_p^n(L_p + l)$ is the overall plume radioactivity depletion on the path length L_p+l given by (4.1).

4.3 Depletion of radioactivity in air during the convective progression over the terrain

A detailed review of relevant parameterisations for modelling of the depletion mechanisms is widely documented. For this study, the models for the dry deposition velocities and the wet scavenging based on the field measurements were compiled. A review of parameterisation for modelling of dry deposition and scavenging of radionuclides is, e.g., in *(Sportisse, 2007)*.

4.3.1 Depletion of the drifted puff due to radioactive decay

The radioactive decay occurs in the entire puff volume. The corresponding depletion along the path of the p^{th} phase is defined as $exp\left(-\lambda^n \frac{l_p}{|\vec{u}_p|}\right)$, where l_p is a straight line of the puff in the hourly phase *p*. In total, the depletion of the puff on its path from beginning up to the end of the phase *p* can be expressed as

$$f_R^n(L_p) = \prod_{k=1}^{k=p} exp\left(-\lambda^n \frac{l_k}{|\vec{u}_k|}\right) \quad , \tag{4.4}$$

where λ^n [1/s] denotes the constant of the radioactive decay of the n^{th} radionuclide.

4.3.2 Depletion of radioactivity due to dry deposition (fallout)

The dry deposition removes pollutants by sedimentation under gravity, by diffusion processes or by turbulent transfer resulting in impacts and interceptions. The radioactivity propagation over the ground enters the source depletion model. The model roughly assumes

that the depletion occurs over the entire depth (vertical column) rather than at the surface. The puff's vertical profile is then distance-invariant, *(Hanna et al., 1982), (Sportisse, 2007*). Due to this simplification, the activity concentrations along the axis can be overestimated.

Let assume the transport in the p^{th} phase runs according to Fig. 4. The term $f_F^n(L_p + l)$ from Eq. (4.1) standing for the fallout depletion in the puff during the whole convective phase should be determined. The amount of radioactivity in the m^{th} puff just entering the phase p is labelled as Q^n_{m,L_p} . Its concentration $C^n_{m,p}(l=0;r,z)$ is expressed by Eq. (4.3). For $p=1$, the amount $Q^n_{m,p=1}$ means the radioactivity just at T^{CALM}_{END} . The term $C^n_{m,p=1}(r,z)$ is a particular component $C^n_{m,I(m)}(r,z)$ from Eq. (3.1). We analyse the fallout during the transport at p^{th} phase in the interval $l \in \langle 0;\ l_p \rangle$, when the centre of the puff is moving linearly with velocity $\vec{u}_p$ along the abscissa $S_{p-1}S_p$, see Fig. 4. For the m^{th} puff at the position l, the radioactivity deposition flux over the ground from the entire puff $\dot{\Omega}^n_{m,p}(l\,; z=0)$ [Bq/s] is

$$\dot{\Omega}^n_{m,p}(l;\, z=0) = vg^n_p(l)\cdot \int_0^{\infty} C^n_{m,p}(l\,;\, r, z=0)\cdot 2\pi\cdot r\cdot dr\,. \tag{4.5}$$

The near-ground activity concentration $C^n_{m,p}(l\,; r, z=0)$ in the interval $l \in \langle 0;\ l_p \rangle$, changing according (4.3), is substituted into (4.5). After the puff shift $dl = u_p\ dt$, the source of radioactivity depletes according to

$$\frac{dQ^n_{m,p}(l)}{dl} = \frac{dQ^n_{m,p}(t)}{u_p\cdot dt} = -\ \dot{\Omega}^n_{m,p}(l;\, z=0)\,. \tag{4.6}$$

For brevity, after substitution, the final integration over l is conducted within the interval $\langle L_p;\ L_{p+1} \rangle$. This gives the partial depletion factor $f_F^n(p)$ on the p^{th} phase. The final form of the total dry-deposit depletion factor for the m^{th} puff, from its entrance to the convective region until the p^{th} phase (including), is given by the product

$$f_F^n(L_{p+1}) = Q^n_{m,p+1} \Big/ Q^n_m\left(T^{CALM}_{END}\right) = \prod_{k=1}^{k=p} f_F^n(k). \tag{4.7}$$

Subdivision on partial depletion factors $f_F^n(p)$ is not autotelic. It has far-reaching implications. The factor $vg^n_p(l)$ in (4.5) strongly depends on the spatial land use categories and radionuclides' physical-chemical forms. They enter processing as environmental gridded data distributed on the fine discrete polar computational grid, as indicated on Fig. 4. The categories reflect the considerable impact of the land use on radioactivity propagation in the living environment. Through the adopted modelling way, the identification between relative coordinate l and respective absolute land use gridded coverage on the real terrain is established and put into operation.

4.4 Depletion of radioactivity in the course of the convective transport due to washout by atmospheric precipitation

Similarly to Sec. 2.6, we assume rain of a constant precipitation rate $\upsilon_{m,p}$ [mm.h^{-1}] during the p^{th} convective phase. The deposition activity rate of n^{th} radionuclide, while washed out from the cloud, is expressed with the aid of the washing (scavenging) coefficient

$\Lambda^n_{m,p} = a \cdot (\upsilon_{m,p})^b$ [s^{-1}]. The precipitation rate $\upsilon_{m,p}$ is averaged over the entire p^{th} convective phase. Likewise (2.8), the wet deposition flux $\dot{W}^n_{m,p}$ [Bq/s] of n^{th} nuclide from the entire m^{th} puff, with its centre at the relative position l of the phase p, is

$$\dot{W}^n_{m,p}(l) = \Lambda^n_{m,p} \cdot \int_0^\infty \left[\int_0^\infty C^n_{m,p}(l\,; r, z) \cdot dz \right] \cdot 2\pi \cdot r \cdot dr \qquad (4.8)$$

The depletion of radioactivity during a differential shift $dl = u_p\, dt$ of the puff (with its centre at the relative position of l) is

$$dQ^n_{m,p}(l) \big/ dl = 1 \big/ u_p \cdot\ dQ^n_{m,p}(l) \big/ dt = -\dot{W}^n_{m,p}(l). \qquad (4.9)$$

For brevity, after substitution and integration over $l \in < 0;\ l_p >$, we obtain expression for a partial source depletion of the radioactivity in the air at the rainy phase p. It is defined as $f^n_w(p) = Q^n_{m,p}(L_{p+1}) \big/ Q^n_{m,p}(L_p)$. The total depletion of the m^{th} puff of the n^{th} radionuclide from its entrance to the convective region until the p^{th} phase (including) is given

$$f^n_W(L_p) \;=\; Q^n_{m,p} \big/ Q^n_m\left(T^{CALM}_{END}\right) \;=\; \prod_{k=1}^{k=p} f^n_W(k) \qquad (4.10)$$

A strong dependency of $\Lambda^n_{m,p}$ on rain intensity brings again far-reaching implications for the rainy phases. An intensive washout could initiate formation of the hot spots of the deposited radioactivity on the terrain. This dangerous phenomenon is shown in the experimental part.

5 Experiments and their results

The trajectory generation of radiological fields in the low wind speed area immediately coupled with a convective transport of the accumulated radioactivity heap is described. The possible serious impact of atmospheric precipitation on incidence of dangerous "hot-spots" of deposited radioactivity on terrain is shown. Continuous release of radionuclides is treated as a sequence of discrete Gaussian puffs from the elevated source.

The experiments compare the fast calculation with the approximation based on Bayes' paradigm (*AB*) with the accurate, but time-consuming, Brute-force (*BF*) solution. The use of *AB* instead of *BF* is tested for a constant and serrated discharges of the source-strength $S^n(t)$. All runs were normalised to the same value *6.0 E+07 Bq* of the total radioactive discharge released into the calm region, see Eqn. (5.1). Convergence of *AB* statistics for an increasing number of discrete puffs M was tested.

5.1 Two consecutive stages of numerical experiment

A hypothetical release of radionuclide ^{137}Cs is divided into two stages. In the first five hours, a calm meteorological state is assumed according to Tab. 1. The total inventory of radionuclide ^{137}Cs is Q^n_{TOT} = *6.0 E+07 Bq*. It is discharged into the motionless ambient air during the calm conditions lasting T^{CALM}=5 hours, $T^{CALM} = \left(T^{CALM}_{END} - T^{CALM}_{START}\right)$. The release is modelled as a sequence of M instantaneous discrete discharges, the first for *m=1* at time T^{LEAK}_{START}, the last for *m=M* at time T^{LEAK}_{END}, according to Fig. 2. The release propagates from the elevated point source of pollution at height *H (x=0; y=0; z=H)* over the terrain. The

radioactivity progresses during the calm episode time interval $\left\langle T_{START}^{CALM}; T_{END}^{CALM} \right\rangle$ according to Fig. 2. The chain of consecutive discrete puffs Q_m^n of ^{137}Cs, $m \in \{1,...,M\}$, are ejected stepwise with the time periods Δt_m. For the case "*constant"* from Fig. 5 the puffs are regularly distributed with the period $\Delta t_m = T^{CALM}/M$. The release-source strength Q_{TOT}^n/M is firstly assumed to be constant within the whole calm episode, see Fig. 2. Other shapes of the source strength are also treated, see below on Fig. 5. After five hours of the calm episode, the wind starts to blow. The convective transport of the radioactivity clew immediately arises. Meteorological records are extracted from stepwise forecast series for the given point of radioactive release. Hourly meteorological data of the convective transport immediately following the five hour calm episode are included in Tab. 2 extending Tab. 1.

Tab. 2: Convective transport (continuation of the calm episode from Tab. 1). Archived meteorological data at (49° 05′ 00.73″ N, 16° 07′ 26.95″ E) of the Dukovany nuclear power plant: start at Dec 4, 2019, 01.00 CET (time_stamp 2019120401). Rain in the 4th convective hour was chosen deliberately for demonstration purposes.

time_stamp yyyymmddhh	Pasquill_cat. (**)	mean wind speed at 10 m height [m.s^{-1}]	wind_direction [°]*	rain [mm.h^{-1}]
.....	.....	.....	.....	.....
2019120401	...F...	..1.8....	345.0	0.0
2019120402	...F...	..3.2....	312.0	0.0
2019120403	...F...	..2.2....	280.0	0.0
2019120404	...F...	..2.2....	260.0	1.0
.....	.....	.....	.....	.....

* Clockwise, from the North (**) Pasquill atmospheric stability class

Three analysed variants of the release source strength $S^n(t)$ shape are in Fig. 5: constant form (Case 1) and serrated forms with two notches and one notch (Case 2 and Case 3). All three runs are normalised to the same value *6.0 E+07 Bq* of the total radioactive discharge Q_{TOT}^n released into the calm region:

$$Q_{TOT}^n = \int_{T_{START}^{LEAK}}^{T_{END}^{LEAK}} S^n(t)\,dt\,. \tag{5.1}$$

$S^n(t)$ [Bq/s] is the source strength from elevated source at height *H, (x=0; y=0; z=H).*

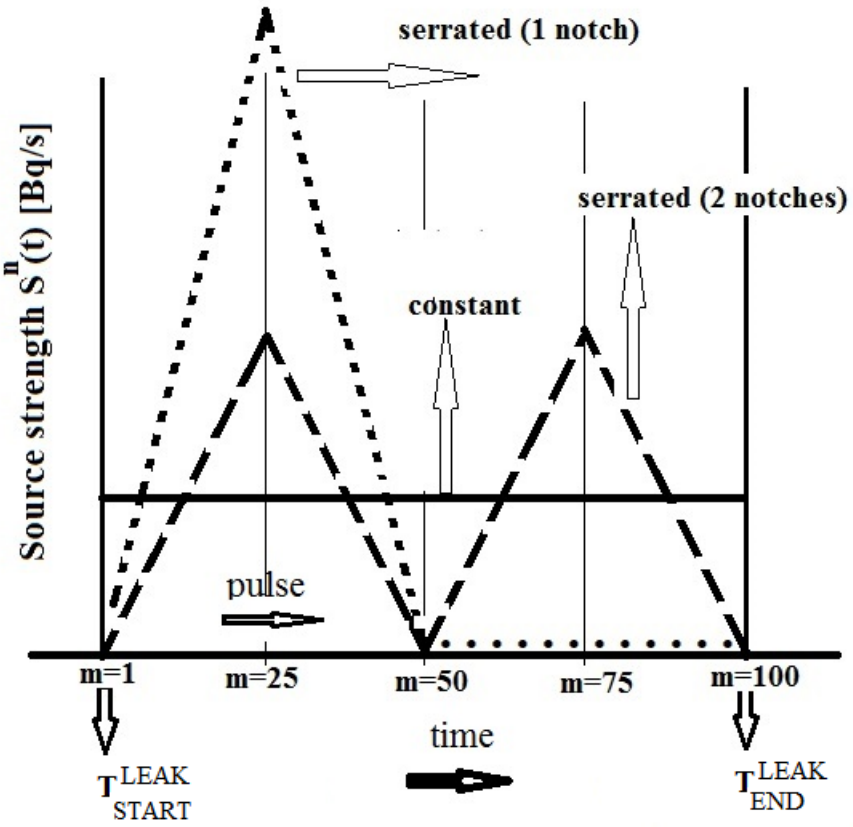

Fig. 5: The release source strength $S^n(t)$ [Bq.s^{-1}] for Case1 (constant shape), Case 2 (serrated, 2 notches) and Case 3 (serrated, 1 notch).

5.2 Demonstration of possible dangerous effect of atmospheric precipitation

A. Constant release source strength shape: Case 1 from Fig. 5:

The results of several tests displayed on the map background of the Czech nuclear power plant at Dukovany are in Fig. 6. The left panel shows the radioactivity propagation in the first stage of the numerical experiment, in the calm region. The right panel displays outcomes of the further convective transport.

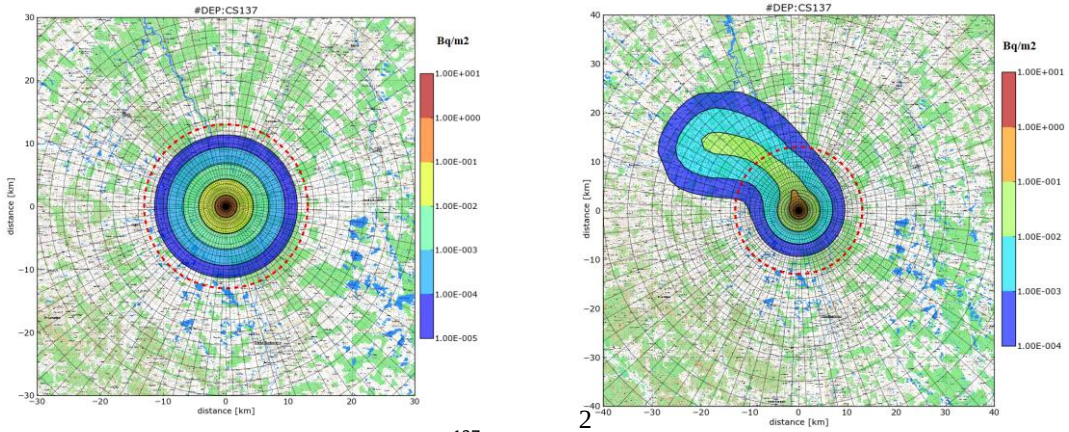

Fig. 6. Deposition of the radionuclide ^{137}Cs on terrain. No atmospheric precipitation, *M=100*, *BF* solution. Left panel: Detailed image of the deposition in the calm region in the emergency planning zone just after 5 hours of the calm episode. Right: Deposition from a further propagation after the successive 4 hours of the convective transport.

Figs. 7 and 8 show the occurrence of red patches of the higher level of deposited radioactivity in the fourth (last) rainy phase of the convective transport. Fig. 7 reflects to Case 1 with the constant source strength, Fig. 8 deals with Case 3 with the serrated shape of the source strength with one notch. The scavenging of radioactive aerosols due to the rainout and washout are lumped together through the scavenging coefficient.

The results on Figs. 7 and 8 demonstrate strong radiological impact of the atmospheric precipitation on the living environment. In comparison with the outcomes with no rain (Fig. 6), the "hot spot" radioactivity deposition values in the region of rain shown on Fig. 7 are increased more than by one order of magnitude, even at the distances of tens kilometres from the pollution source.

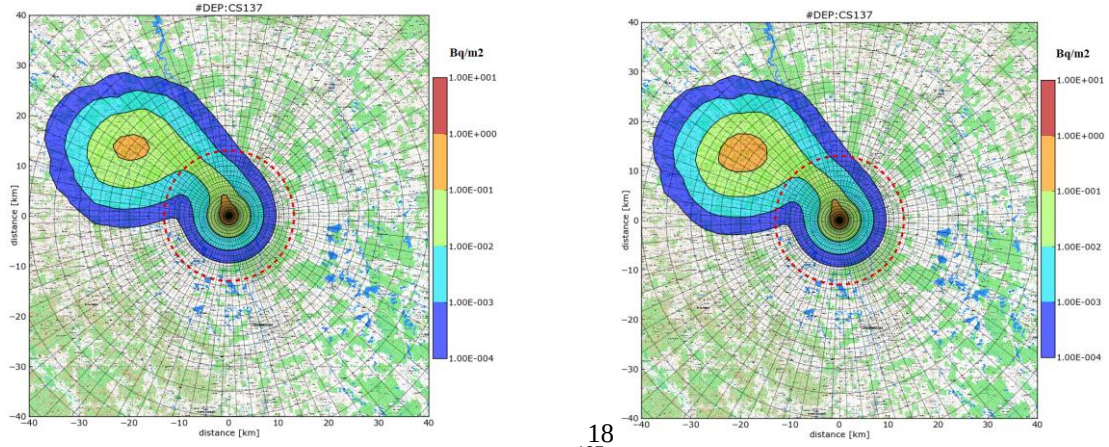

Fig. 7. "Hot spots" of deposited radionuclide ^{137}Cs on terrain. *M=100*, *BF* solution, the release source of a constant strength. The atmospheric precipitation in the fourth hour of the convective transport causes the serious increase of the deposited activity ^{137}Cs. Left: Results for the rain with the intensity *1.0 mm.h*$^{-1}$. Right: Rain with the higher intensity *2.0 mm.h*$^{-1}$.

B. Serrated release source strength shape: Case 3 from Fig. 5.

Discharges of the Case 3 are concentrated in the first phase of the release. They are dispersing a longer time until the calm end. The maximum concentration is then decreased and its 2-D trace is flattened. The situation on the polar grid is drawn on Fig. 8. Polar grid representation in Figs 8, 9 is as follows: Radius: 42 concentric circles up to 100 km from the source; Azimuth: 2π radians split to 80 regular radial beams 1÷80. They are numbered clockwise from north.

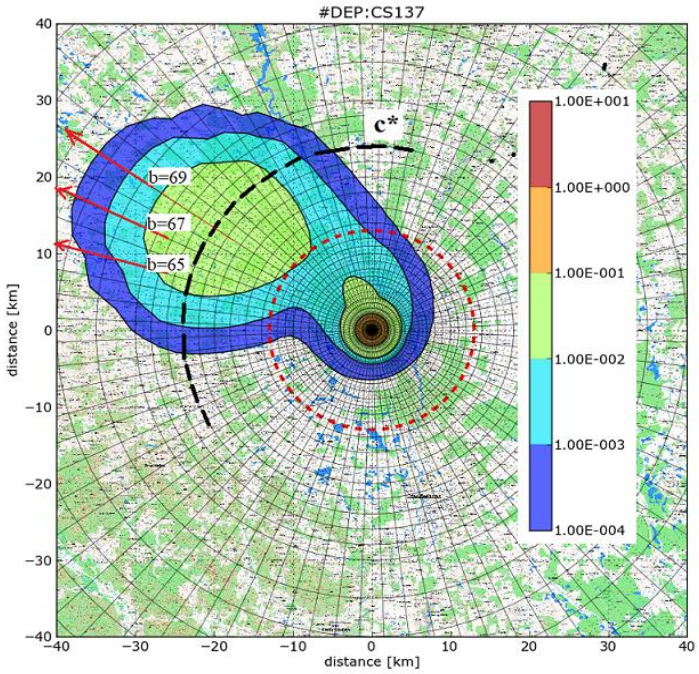

Fig. 8: "Hot spots" of deposited radionuclide ^{137}Cs on terrain. *M=100*, *BF* solution, serrated release source strength (Case 3 from Fig. 5: the serrated shape with one notch). Atmospheric precipitation with intensity *1.0 mm.h*$^{-1}$ in the fourth hour of the convective transport.

5.3 Validity tests of the proposed approximation based on Bayes' paradigm *AB*

The applicability of super-puff Gaussian approach heavily depends on the approximation quality: its errors must be sufficiently small. Extensive numerical experiments confirm the acceptability of the *AB* procedure under the inspected circumstances. The use of a large puff number *M* makes modelling quite flexible and allows us to follow a continuous release of significantly varying properties. The proposed feasible approximation *AB* by a single Gaussian super-puff, described in Sec. 3, decreases the excessive computational load connected with a high *M* but it brings an approximation error into the processing. Thus, it is necessary to compare its quality with the results obtained without it, with the results obtained by the *BF* procedure, see Sec. 4.1.

Practically, procedures *AB* and *BF* provide different initial conditions of the radioactivity distribution just at the moment T_{END}^{CALM} for the ensuing convective transport. The values of radiological impact calculated in the further convective transport for two different initial conditions *BF* and *AB* and for various numbers *M* of discrete puffs of radioactive discharges are compared. The consensus between the respective values of the deposited radioactivity on the ground is inspected. The differences are expected to be most visible and critical, see Sec. 5.2, in the fourth convective phase under the rain.

5.3.1 Comparison for Case 1 and a large number of discrete puffs, *M*=100

The experimental conditions correspond with the scenario of radioactive release given in Sec. 5.1 for the constant source strength, Case 1 in Fig. 5.

The results for the *BF* calculation runs with *M=100* puffs and the rain intensity *1 mm.h*$^{-1}$ in the fourth convective phase is drawn above on Fig. 7 in its left panel. The figure is redrawn on

Fig. 9, the right panel, where a specific *circle c** and *beam b** of the computational grid are highlighted. They serve for a detailed comparison of the inspected procedures.

The same scenario for the *AB* calculation run is on the left panel of Fig. 9. Respective parameters (covariance matrix based on (3.4)) of the super-puff Gaussian distribution $C^n\left(T_{END}^{CALM};r,z\right)^{TOTAL}$ was generated in advance (from the previous *BF* calculations for the calm region) as ${}^{AB}\sigma_r = 2.039E{+}03\ m$, ${}^{AB}\sigma_z = 9.204E{+}02\ m$, $Fdepl^{opt} = 0.9338$ stands for sum of component weights (fallout) , see also Tab. 3, below.

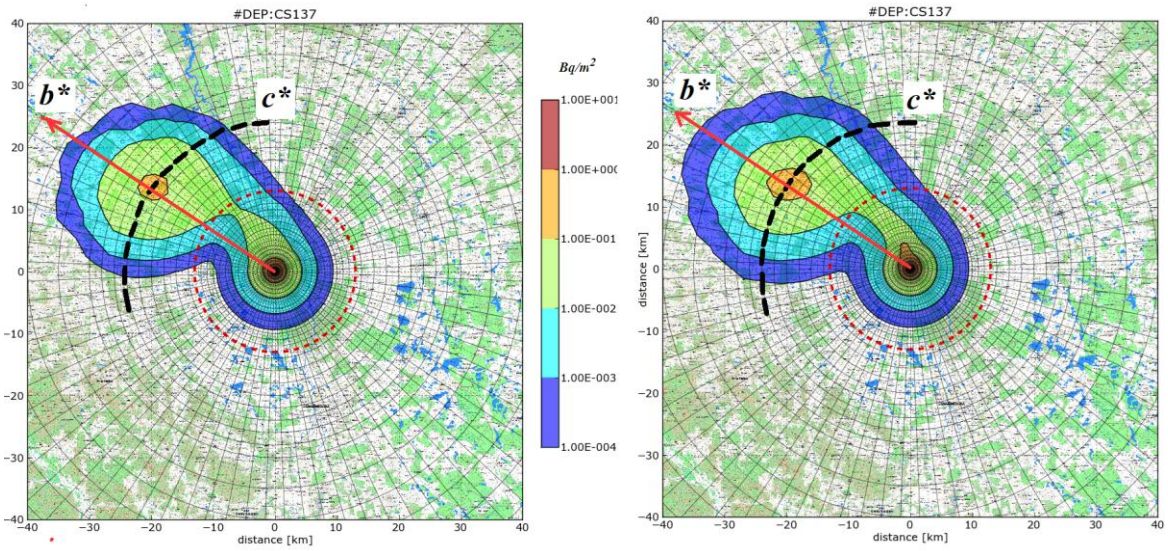

Fig. 9: The results for $M{=}100$ for algorithms *AB* (Left) and *BF* (Right). The release scenario with the rain with intensity $1\ mm{\cdot}h^{-1}$ in the fourth phase (hour) of the convective transport. The peripheral circle *c** and the radial beam *b** of the polar computational grid are sketched.

2-D comparison of *BF* with *AB* is in Fig. 9. For this simple scenario, the values are close each other and the differences can hardly be noticed. A more detailed graphical comparison of the computational procedures *BF* and *AB* are in Figs. 10a, 10b and 11. Computed deposition values are arranged along the peripheral (circle *c**) and the radial (beam *b**) paths.

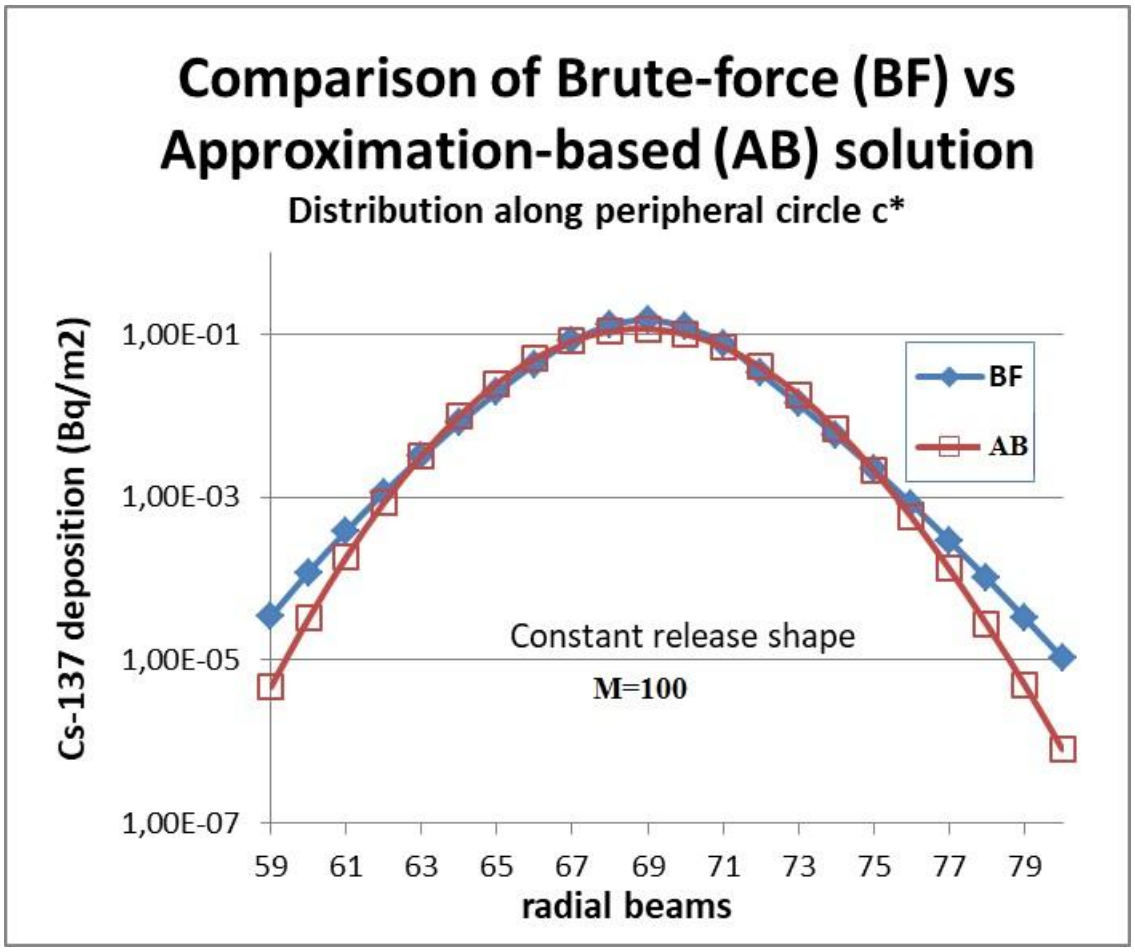

Fig. 10a: The distribution of ^{137}Cs deposition on the ground along the peripheral direction along the circle c^* with diameter *25 km* from the source as a function of the radial polar beams around beam *b*=69* (sketched in Fig. 9). The values concern the fourth rainy phase with the rain intensity *1 mm.h*$^{-1}$.

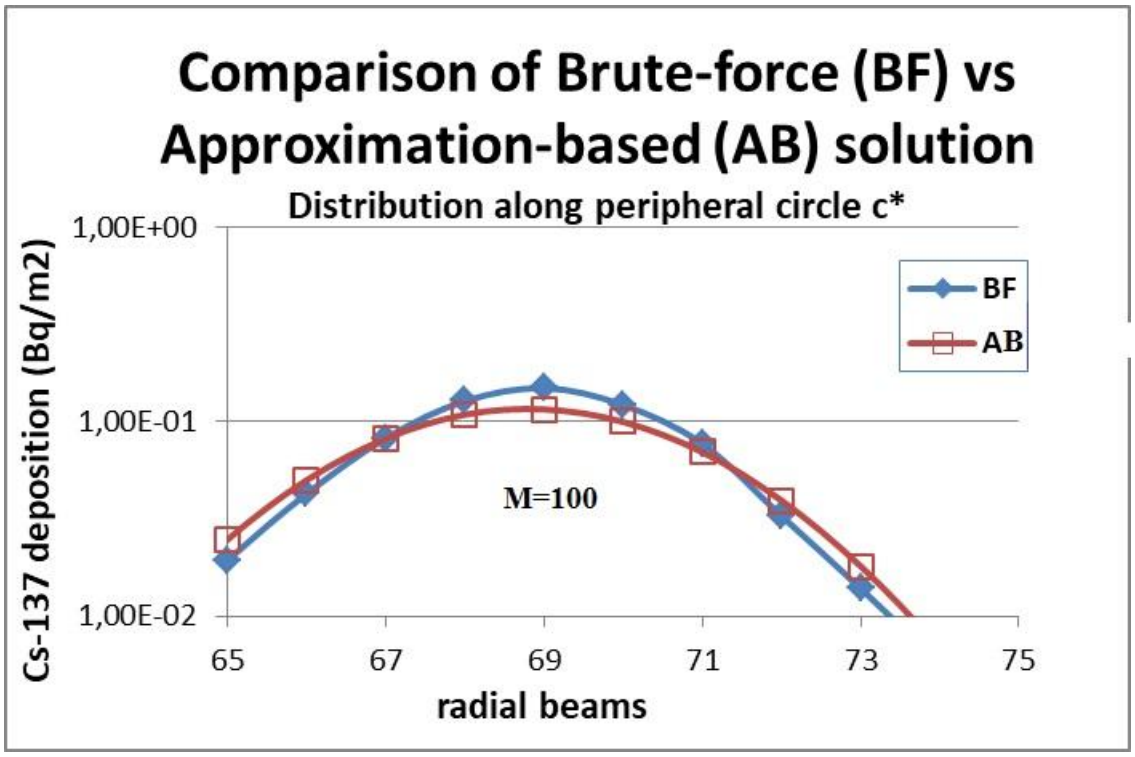

Fig. 10b: Zoom in the central region of Fig. 10a. Distribution of ^{137}Cs deposition on the ground along the peripheral direction along the circle c* with diameter *25 km* from the source as a function of the radial polar beams around beam *b*=69* (sketched in Fig. 9).

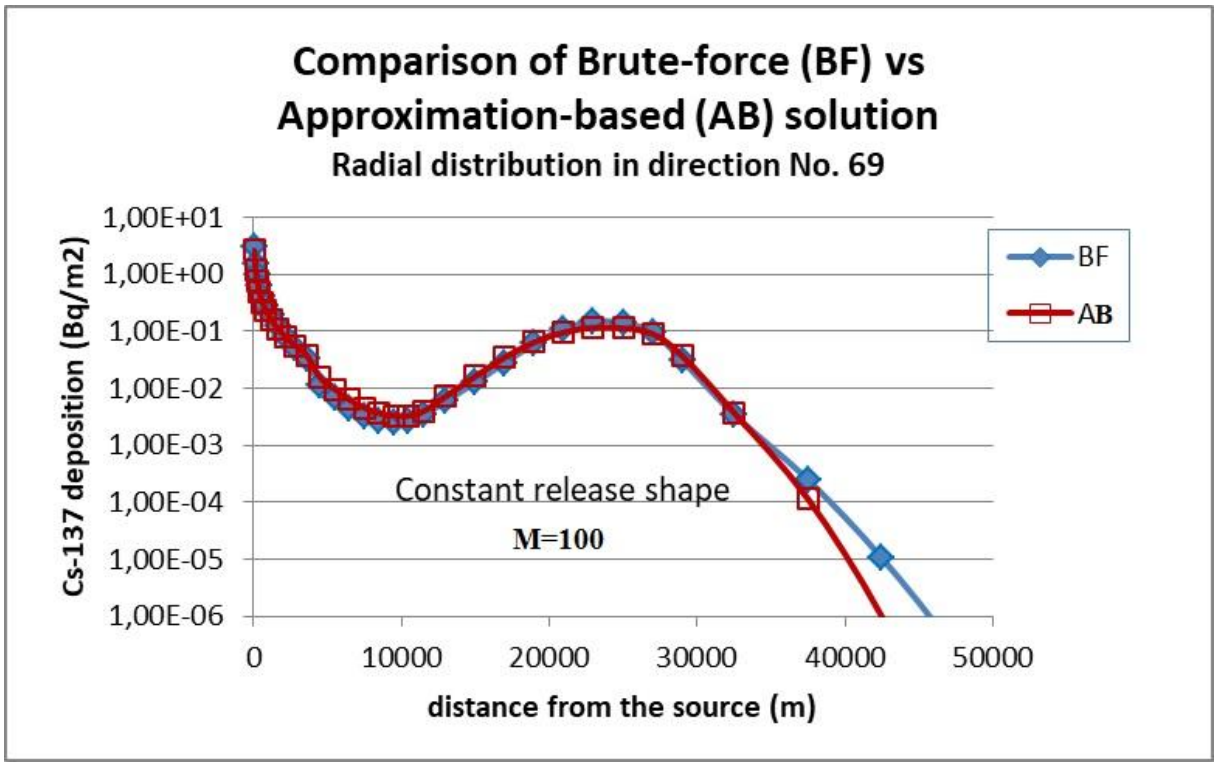

Fig. 11: The distribution of ^{137}Cs deposition on the ground in the radial direction along the beam *b*=69* (shown in Fig. 9). The values concern the 4th rainy phase with the rain intensity *1 mm.h^{-1}*.

5.3.2 Comparison of *AB* and *BF* solutions for varying source strengths, Cases 2, 3

Having in mind the normalisation (Eq. 5.1), the Case 3 (serrated, 1 notch) differs from Case 1 (constant shape). The Case 2 (serrated, two notches) lies about in the middle of these cases. A more detailed graphical comparison of the computational procedures *BF* and *AB* for serrated 1 notch is given on Fig. 12. The explanation of closer *BF* and *AB* values results from the fact that 1 notch from Case 3 disperses for a longer time in the calm region (see also the radioactivity decrease in Fig. 8). The heavy tail of the non-Gaussian *BF* solution is visible at the border of the outlined region. The values of both variants for the important inspected central region are close each other.

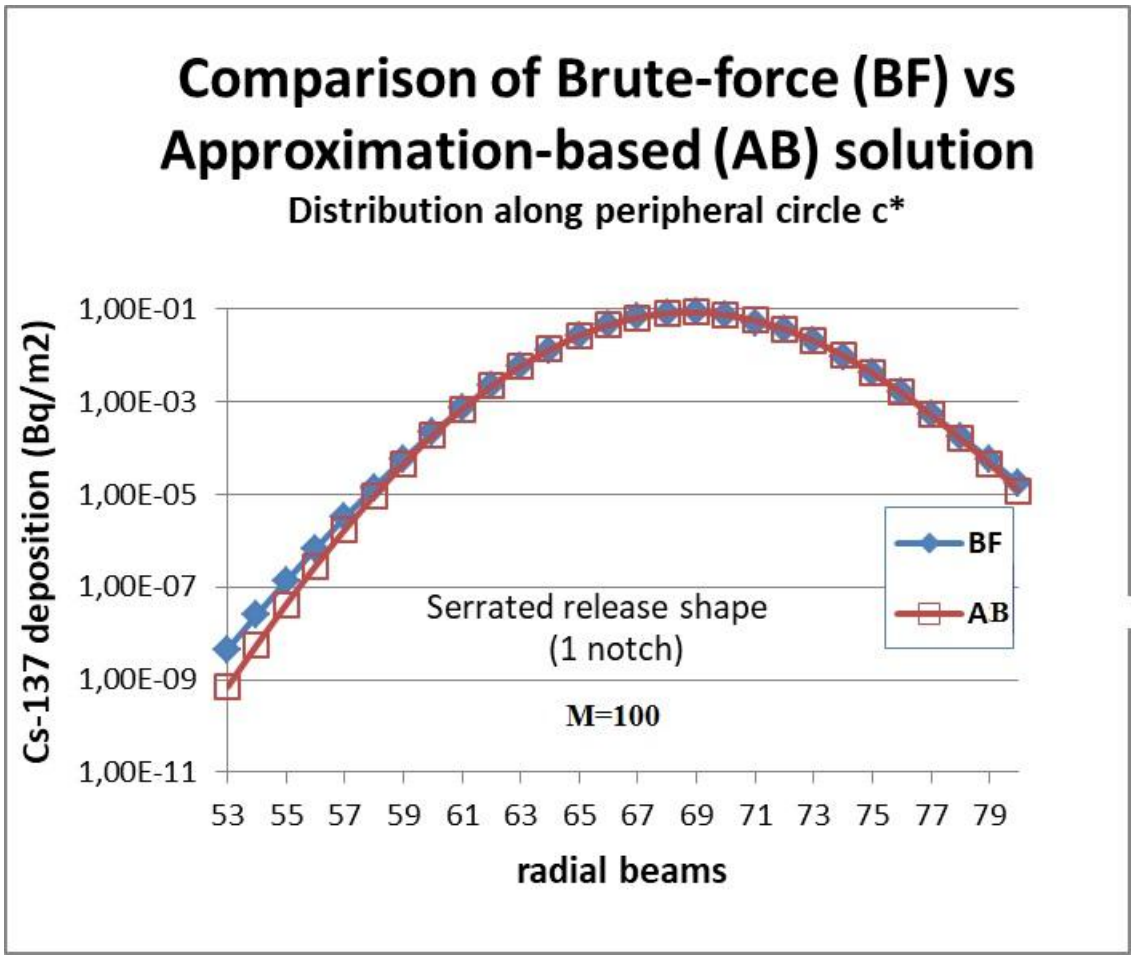

Fig. 12: The distribution of ^{137}Cs deposition on the ground in peripheral direction along the circle c* with diameter *25 km* from the source as a function of the radial beams around beam *b*=69* (sketched in Fig. 9). The values belong to the fourth rainy phase with the rain intensity *1 mm.h*$^{-1}$.

5.3.3 Dependency of the *AB* solution on the number of discrete puffs *M*

The procedure *AB* is introduced in Sec. 3.1 with the aim to approximate the Gaussian mixture (3.1) by a single Gaussian super-puff distribution. Quality of the *AB* approximation naturally depends on the total number of processed discrete puffs *M* and has to be inspected. The representative results of extensive computational runs doing this are in Tab. 3.

Tab. 3: Gaussian super-puff approximation *AB* of the real Gaussian mixture (3.1).
Fdepl^{opt} stands for sum of component weights (fallout).

	Statistical parameters of super-puff Gaussian

The release shape	M -	approximation AB $Fdepl^{opt}$ -	σ_r^{opt} [m]	σ_z^{opt} [m]
constant (1)	10	0.9197	2.166 E+3	9.759 E+2
constant (1)	100	0.9338	2.039 E+3	9.204 E+2
serrated- 2 notches (2)	100	0.9377	2.022E+3	9.129E+2
serrated- 1 notch (3)	100	0.8999	2.734E+3	1.233E+3
constant (1)	200	0.9345	2.034 E+3	9.172 E+2
constant (1)	300	0.9347	2.031 E+3	9.161 E+2

(1) Case 1: constant shape from Fig. 5;
(2) Case 2: serrated shape (2 notches) from Fig. 5;
(3) Case 3: serrated shape (1 notch) from Fig. 5;

Tab. 3 supports the conjecture that the solution is not too much sensitive to the number of puffs and, importantly, it convergences for $M \to \infty$ (continuous release).

6 CONCLUSIONS

Discharges of the radioactivity into the motionless ambient atmosphere can cause a significant radioactivity accumulation near the source of pollution. The situation pertains to the "worst case" scenarios, which are examined within WVA (Weather Variability Assessment) analysis. Significant extent of involved uncertainties reduces credibility of the model predictions. Solution offers the data assimilation techniques accounting for the real measurements incoming from terrain. This approach decreases the degree of uncertainty of results and allows generate probabilistic answers to assessment questions. Data assimilation methods pay attention to chaotic nature of atmosphere that imposes limit on the stability of weather predictions and weather predictability at all. The techniques have been found as an efficient tool in the struggle against tendency to destruction of model knowledge.

The results of this article can be understood as an effort to develop a fast and efficient realistic tool supporting the data assimilation applications. An experience from analysis of the regional-scale atmospheric dispersion of Fukushima Dai-ichi nuclear power plants accident has been utilized *(Terada et al., 2012)*. This article follows-up the earlier foregoing concise work *(Pecha et al., 2020)* dealing with generation of the prior knowledge radiological fields of the minor calm scenario. An original approach is proposed providing a sufficiently accurate estimate of the statistical properties of the originally non-Gaussian sum of discrete Gaussian puffs from the calm region. It approximates the sum in Eq. (3.1) by a single super-puff distribution of the Gaussian type. Instead of many calculation runs of the successive convective transport for each individual puff (brute-force procedure, *BF*), only one super-puff run can be realised (approximation based on Bayesian paradigm, *AB*). It brings substantial benefits in acceleration of multi-fold generation of the complex radiological trajectories (usually thousands of computation runs) coupling the calm and convective regions with *AB* approximation.

The results in Section 5.2 show a significant increase of radioactivity - especially, in combination with rain. The rainy scenario may lead to appearance of considerable radioactivity hot spots rather far from the release source. Detailed results of comparative

analysis of the *AB* vs *BF* solutions are given in Section 5.3. A good consent is found for tested variants. It relates to comparison of miscellaneous complex trajectories of radiological fields in the low wind speed area coupled with the immediate convective transport (with or without rain). Moreover, the tests of various shapes of the release source strength and convergence of the *AB* statistics for high number of discrete discharges *M* have been successfully accomplished.

From the software point of view, the article introduces original algorithm for true embodiment of the atmospheric changes during progression of each individual pulse (detailed described in Figure 2). However, the main contribution to methodology lies in derivation of the novel approximation based solution *AB* and its introduction into operation. It favourably affects three important areas concerning: a) feasibility of prospective computationally intensive Bayesian methods of data assimilation; b) generation of a simple initial conditions in the form of optimal Gaussian approximant given by Eq. (3.4), which initiates the convective radioactivity transport for applications of the advanced dispersion codes; c) capability to perform full range uncertainty and sensitivity analyses thus forming a proper basis for advanced probabilistic consequence assessments.

The methodology proposed in this article is supported by detailed complementary study (*Pecha and Kárný, 2021*) demonstrating improved feasibility of the joint uncertainty and sensitivity analyses performance of the complex calm scenario utilising random sampling techniques.

ACKNOWLEDGEMENTS

The authors are grateful to the IT department of the National Radiation Protection Institute in Prague for free access to the archives of the historical meteorological data. The research of MK was partially supported by MŠMT ČR LTC18075 and EU-COST Action CA1622. Dr. T.V. Guy provided us a useful feedback on the presentation way.

REFERENCES

Adriaensen, S., Cosemans, S., Janssen, L. and Mensink, C. (2002): PC-Puff: A simple trajectory model for local scale applications. *Risk Analysis III, CA Berbia (Ed.). ISBN 1-85312-915-1.*

Baklanov, A. and Sorensen, J.H. (2001): Parametrisation of Radionuclide Deposition in Atmospheric Long-Range Transport Modelling. *Phys. Chem. Earth, 26(10).*

Bernardo, J. (1979): Expected Information as Expected Utility. *The Annals of Statistics, **7**, pp. 686 – 690.*

Brioude, J., Arnold, D., Stohl, A., Cassiani, M., Morton, D., Seibert, P., Angevine, W., Evan, S., Dingwell, A., Fast, J. D., Easter ,R .C., Pisso, I., Burkhart, J. and Wotawa, G. (2013): The Lagrangian particle dispersion model FLEXPART-WRF version 3.0. *Geosci. Model Dev. Discuss., **6**, pp. 3615–3654.*

Carruthers, D. J., Weng, W. S., Hunt, J.R.C., Holroyd, R.J., McHugh, C.A. and Dyster, S.J. (2003): PLUME/PUFF Spread and Mean Concentration - Module Specifications. *ADMS4 paper P10/01S/03, P12/01S/03.*

EPA (2004): AERMOD: Description of Model Formulation. *U.S. Environmental Protection Agency, Research Triangle Park, NC (Report EPA-454/R-03-004).*

McGuire, S.A., Ramsdell, J.V. and Athey, G.F. (2007): RASCAL 3.0.5: Description of Models and Methods. *NUREG – 1887.*

HARP (2010-2019): Environmental SW package HARP (**HA**zardous **R**adioactivity **P**ropagation). *(HARP, 2010-2019).*

Hanna, R.S., Briggs, G.A. and Hosker (Jr.), R.P. (1982): Handbook on Atmospheric Diffusion. *DOE/TIC-11 223, (DE82002045).*

Hershey J.R., Olsen P.A. (2007): Approximating the Kullback Leibler Divergence Between Gaussian Mixture Models, *ICASSP '07, Honolulu, HI, pp. IV-317-IV-320.*

Horst, T.W. (1977): A Surface Depletion Model for Deposition from a Gaussian Plume. *Atmospheric Environment, **11**, pp. 41-46.*

Hyojoon, J., Misun, P., Wontae, H., Enuhan, K. and Moonhee, H. (2013): The effect of calm conditions and wind intervals in low wind speed on atmospheric dispersion factors. *Annals of Nuclear Energy, **55**, pp. 230-237.*

Jones, J.A. (1996): Atmospheric Dispersion at Low Wind Speed. *Liaison Comm. Annual Report, 1996-1997, ANNEX A, NRPB-R292.*

Kahl J.D.W., Chapman, H.L. (2018): Atmospheric stability characterization using the Pasquill method: A critical evaluation, *Atmospheric Environment, **187**, pp. 196-209.*

Kárný, M., Guy, T.V. (2012): On Support of Imperfect Bayesian Participants. In: Guy T.V. et al, Decision Making with Imperfect Decision Makers, *Springer, Intelligent Systems Reference Library, **28**, pp. 29 – 56.*

Kullback, S., Leibler, R. (1951): On information and sufficiency. *The Annals of Mathematical Statistics, **22**, pp. 79 – 87.*

Lines, J.G. and Deaves, D.M. (1997) : The implication in dispersion in low wind speed condition for qualified risk assessment. *WS Atkins Consult., WSA/RSU 8000/035.*

McLachlan, G.J., Peel D. (2000): Finite Mixture Models, *Wiley Series in Prob. and Stat.*

Okamoto, S., Onishi, H., Yamada T., Mikami, T., Momose, S., Shinji, H. and Itohia, T. (2001): A Model for Simulating Atmospheric Dispersion in a Low wind Condition. *Int. J. Environment and Pollution, **16**.*

Pandey, G. and Sharan, M., (2019). Accountability of wind variability in AERMOD for computing concentrations in low wind conditions. *Atmospheric Environment **202**, pp. 105–116.*

Park, S.-U., Lee, I.-H., Joo, S.J., Ju, J.-W. (2017): Emergency preparedness for the accidental release of radionuclides from the Uljin Nuclear Power Plant in Korea. *Journal of Environmental Radioactivity, Volume 180, December 2017, Pages 90-105.*

Pecha, P., Kárný, M. (2021): Improved Feasibility of Joint Uncertainty and Sensitivity Analyses Performance for Complex Scenario of Accidental Radioactivity Release into the Calm Atmosphere. *Draft, submitted for publication*.

Pecha, P., Tichý, O., Pechová, E. (2020): Determination of Radiological Background Fields Designated for Inverse Modelling during Atypical Low-Wind Speed Meteorological Episode. *J. Atmospheric Environment*, **246**, 2021, 118105.

Pecha, P. and Šmídl, V. (2016): Inverse modelling for real-time estimation of radiological consequences in the early stage of an accidental radioactivity release. *Journal of Environmental Radioactivity, **164**, pp. 377-394.*

Pöllänen, R., Toivonen, H., Lahtine, J. and Ilander, T. (1995): Transport of Large Particles Released in a Nuclear Accident. *STUK-A125.*

Rakesh, P.T., Venkatesan, R., Srinivas, C.V., Baskaran, R. and Venkatraman, B. (2019): Performance evaluation of modified Gaussian and Lagrangian models under low wind speed: A case study. *Annals of Nuclear Energy **133**, pp. 562–567.*

Sportisse, B. (2007): A review of parameterization for modelling dry deposition and scavenging of radionuclides. *Atmospheric Environment **41**, pp. 2683-2698.*

Šmídl, V. and Hofman R. (2013): Adaptive Importance Sampling in Particle Filtering. *Proceeding of the 16th Int. Conf. on Information Fusion, (Istanbul, 09.07.2013-12.07.2013).*

Terada, H., Katata, G., Chino, M. and Nagai, H. (2012): Atmospheric discharge and dispersion of radionuclides during the Fukushima Dai-ichi Nuclear Power Plant accident. Part II: verification of the source term and analysis of regional-scale atmospheric dispersion. *Journal of Environmental Radioactivity, Volume 112, October 2012, Pages 141-154.*

Tsuda, A., Henry, F. S. and Butler, J.P. (2013): Particle transport and deposition: basic physics of particle kinetics. *Compr. Physiol., **3**(4), pp. 1437-1471.*

Zannetti, P. (1990): Air Pollution Modeling. Theories, Computational Methods and Available Software. *ISBN 1 – 85312-100-2.*

Zhang, S., Liu, R. and Zhao, T. (2018): Mapping radiation distribution on ground based on the measurement using an unmanned aerial vehicle. *Journal of Environmental Radioactivity, Volumes 193–194, October 2018, Pages 44-56.*